Unexpected ice-induced vibrations of a conical structure in model scale

Petry, Alice; Puolakka, Otto; Hammer, Tim C.; Hendrikse, Hayo; Polojärvi, Arttu

DOI
10.1016/j.marstruc.2025.103880

Publication date
2025

Document Version
Final published version

Published in
Marine Structures

Citation (APA)
Petry, A., Puolakka, O., Hammer, T. C., Hendrikse, H., & Polojärvi, A. (2025). Unexpected ice-induced vibrations of a conical structure in model scale. *Marine Structures*, *104*, Article 103880. https://doi.org/10.1016/j.marstruc.2025.103880

Marine Structures 104 (2025) 103880

Contents lists available at ScienceDirect

Marine Structures

journal homepage: www.elsevier.com/locate/marstruc

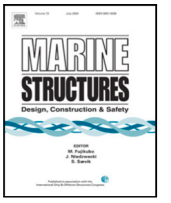

Research paper

Unexpected ice-induced vibrations of a conical structure in model scale

Alice Petry [a,*], Otto Puolakka [a], Tim C. Hammer [b], Hayo Hendrikse [b], Arttu Polojärvi [a]

[a] Aalto University, School of Engineering, Department of Energy and Mechanical Engineering, P.O. Box 14300, FI-00076 Aalto, Finland
[b] Delft University of Technology, Faculty of Civil Engineering and Geosciences, Department of Hydraulic Engineering, Stevinweg 1, 2628 CN Delft, The Netherlands

ARTICLE INFO

Dataset link: https://doi.org/10.5281/zenodo.13899191

Keywords:
Model ice
Hardware-in-the-loop
Offshore structures
Ice-structure interaction
Bending failure
Shear failure

ABSTRACT

Offshore wind turbines in cold sea areas can be fitted with ice cones to reduce static and dynamic loads from drifting sea ice. The effectiveness of ice cones in reducing static loads has been tested in model-scale ice basin experiments. However, only a few experiments used compliant test setups to study ice-induced vibrations on conical structures. This study explores the dynamic interaction between level ice and a downward-bending cone with a 60° slope angle through ice basin tests with a hardware-in-the-loop system based on a hybrid technique, combining a physical indenter with a numerical structure model of an offshore wind turbine. Two types of periodic ice-induced vibrations were observed for the first time in an ice basin: bending failure-induced vibrations and unexpected vibrations caused by local failure at the ice-structure interface. The local failure had characteristics of both shear failure and crushing failure and occurred at low ice-structure interaction speeds during tests. Local failure-induced vibrations were significant in the dynamic test with an ice-drift speed of $5\,\mathrm{mm\,s^{-1}}$, however they also contributed to the dynamic response of the structure at higher ice-drift speeds. Bending failure-induced vibrations occurred at critical ice-drift speeds ($30\,\mathrm{mm\,s^{-1}}$ to $40\,\mathrm{mm\,s^{-1}}$ and $70\,\mathrm{mm\,s^{-1}}$ to $100\,\mathrm{mm\,s^{-1}}$) where the bending failure frequency matched the 1st or 2nd natural frequency of the structure model. The results show that ice-induced vibrations on conical structures occur at various ice-drift velocities for both previously known and unexpected ice failure modes. Furthermore, the results provide new insight into conducting ice basin tests on ice-structure interaction with compliant conical structures.

1. Introduction

Current and future offshore wind farms in northern latitudes, such as the Northern Baltic Sea and the Bohai Sea, need to be designed to withstand sea ice loads. Common substructures, such as monopiles, may not withstand the expected ice loads, for example, in the Northern Baltic Sea [1]. Moreover, offshore wind turbines (OWTs) are slender, compliant structures prone to ice-induced vibrations [2]. Ice cones present a known solution to reducing static and dynamic loads from drifting level ice by shifting the dominant ice failure mode from crushing failure to bending failure.

* Corresponding author.
E-mail addresses: alice.petry@aalto.fi (A. Petry), otto.puolakka@aalto.fi (O. Puolakka), t.c.hammer@tudelft.nl (T.C. Hammer), h.hendrikse@tudelft.nl (H. Hendrikse), arttu.polojarvi@aalto.fi (A. Polojärvi).

https://doi.org/10.1016/j.marstruc.2025.103880
Received 8 October 2024; Received in revised form 22 April 2025; Accepted 8 June 2025
Available online 8 July 2025

Ice cones have been installed on a variety of offshore structures, including bridges and lighthouses [3], OWTs [4–6], and hydrocarbon extraction platforms [7–9]. For example, before the installation of an ice cone, the Kemi-I lighthouse experienced severe vibrations, which led to the failure of structural components. No continuous vibrations were observed after fitting an ice cone [3]. The dynamic excitation of offshore structures with conical substructures was first studied after significant vibrations were observed on the JZ20-2 MUQ platform in the Bohai Sea [8,9]. At high ice-drift speeds, the bending failure frequency of the ice coincided with a natural frequency of the structure, causing large oscillations of the narrow, conical, and flexible jacket structure.

The effectiveness of ice cones has been studied using model-scale ice basin experiments. A review by Wessels and Kato provides an overview of early studies of ice-cone interaction using ice basin tests and theoretical derivations [10]. These studies mainly focused on static load reduction using ice cones [11–14]. Later studies focused on dynamic ice-structure interaction with ice cones [4,7,15,16]. The structural dynamics were modelled using a "compliance simulator", a rigid structure model connected to a compliant support [17]. Only the studies by Huang et al. [15] and Tian and Huang [7] captured a dynamic response. In both studies, dynamic amplification occurred when the ice failed through a two-time bending failure process: first through bending failure of the ice sheet into wedges, then through bending failure of the wedges. The combined frequency of the load peaks caused by both failure events led to high-amplitude structural vibrations. Note that this two-time bending failure is not commonly described in field observations (except occasionally against steep conical structures [18] and the Norströmsgrund lighthouse [19]).

All of the above-cited studies focused on studying dynamic ice-structure interaction in model-scale ice basin tests. These studies used Cauchy–Froude scaling to maintain the relationship between inertial and gravitational forces, as well as inertial and elastic forces. Recent studies on ice-induced vibrations on vertically-sided structures used a novel scaling approach based on the preservation of kinematics during ice-structure interaction [20]. Instead of a "compliance simulator", the experiments used a test setup with a hardware-in-the-loop system based on the hybrid technique [21]. Experimental results, using this test setup, have been verified against full-scale data of the Molikpaq platform and Norströmsgrund lighthouse [20]. The setup also has been used to study ice-induced vibrations on a reference 14 MW OWT [2,22].

Considering the success of the above-mentioned studies on vertical substructures, this paper presents an exploratory study using the same hardware-in-the-loop test setup and structure model of an OWT to analyse ice-induced vibrations on a 60° downward-bending cone. Two types of experiments were performed: rigid tests (no implementation of a structural model in the numerical domain of the hybrid environment) to study the ice failure mechanisms, and dynamic tests (implementation of a structural model in the numerical domain of the hybrid environment) to study ice-structure interaction. The structure model was scaled to facilitate ice-structure interaction rather than to represent the structural dynamics of a reference OWT. Two types of large-amplitude ice-induced vibrations were observed during the experiments: the bending type, as observed on JZ20-2 MUQ, and an unexpected, not previously observed, local failure type with characteristics of crushing and possibly shear failure. This paper presents a qualitative analysis of the observed local failure and bending failure modes and discusses the implications of the observed failure modes for model-scale experiments focused on ice-structure interaction with a compliant conical structure.

2. Methods

The experiments were performed as a part of a larger research project focused on studying ice-induced vibrations on vertically-sided structures. A first test campaign was performed in June 2021 at the Aalto Ice and Wave Tank. This test campaign focused on studying the dynamic response of a vertically-sided offshore wind turbine (OWT) subjected to crushing ice loads [2], as well as the effect of wind–ice misalignment on an OWT [22]. This test campaign made use of a novel test setup using a hardware-in-the-loop system based on the hybrid technique [23]. A second test campaign was performed in April 2023. The second test campaign focused on generalizing the findings from the first campaign and on expanding the research to conical structures. The second test campaign used an improved version of the first test setup [21]. The outcome of the second test campaign was a novel scaling approach to study ice-induced vibrations on vertically-sided structures [20]. An integral part of the scaling approach is the use of a novel type of model ice. This model ice predominantly fails in crushing and exhibits a velocity effect at low ice-drift speeds, similar to sea ice [20].

The experiments presented in this study were performed on April 25, 2023. The experiments used the test setup presented in [21], the model ice presented in [20] and the numerical model of an OWT presented in [2,22]. The experiments also used the scaling approach presented in [20]. While this approach is typically used to scale a structure with a full-scale counterpart in mind [2,22], in this specific study, it is solely used to calibrate the stiffness of the structure model to enable ice-structure interaction. This section describes the model ice, test setup, numerical model of an OWT and the scaling approach used in the experiments with the conical structure.

2.1. Model ice

The Aalto Ice and Wave Tank is a 40 m by 40 m, 2.8 m deep basin equipped with a cooling and spraying system to produce fine-grained model ice. Fine-grained model ice was produced as outlined by Li and Riska [24]: first, water–ethanol mixture was sprayed into the air at an air temperature of −10 °C to create an initial carrying layer. The spraying process then continued for about 225 min until the desired ice thickness of $h = 25$ mm was reached. The temperature was then decreased to −12 °C to allow the ice to harden overnight. The ambient air temperature was maintained at −10 °C during testing. Maintaining a low temperature during the testing day resulted in a type of model ice called "cold model ice". The mechanical properties and ice thickness evolved throughout the testing day because of the low ambient air temperature. The mechanical properties of the ice, as measured at the

Table 1
Elastic modulus E, flexural strength σ_f and compressive strength σ_c of the model ice. The target ice thickness h was 25 mm.

Test time	E [MPa]	σ_f [kPa]	σ_c [kPa]
Around 9:00	2581	464	759
Around 18:00	5012	545	1054

beginning and at the end of the testing day, are presented in Table 1. Local ice thickness measurements were performed after each set of experiments were completed. The local ice measurements are presented in the Appendix (Table A.1). Thin sections of the model ice were presented in [25].

The characteristic length of the model ice can be calculated using expressions based on a semi-infinite beam on an elastic foundation $l_{\mathrm{c,beam}}$ or a semi-infinite plate $l_{\mathrm{c,plate}}$ on an elastic foundation, namely:

$$l_{\mathrm{c,beam}} = \left(\frac{4Eh^3}{12\rho_w g}\right)^{1/4} \text{ and} \tag{1}$$

$$l_{\mathrm{c,plate}} = \left(\frac{Eh^3}{12\rho_w g(1-\nu^2)}\right)^{1/4}, \tag{2}$$

where E is the elastic modulus, h is the ice thickness, ν is the Poisson's ratio of the ice, g is the gravitational acceleration and ρ_w is the density of the liquid water–ethanol solution. The characteristic length of a beam on an elastic foundation with $E = 2.5$ GPa to 5 GPa and $h = 20$ mm to 30 mm is $l_{\mathrm{c,beam}} = 0.91$ m to 1.46 m. The characteristic length of a plate on an elastic foundation is $l_{\mathrm{c,plate}} = 0.93$ m to 1.5 m. The corresponding analytical bending failure length for a beam would be a factor $\pi/4$ smaller than the characteristic length.

2.2. Experimental setup

This study used a hardware-in-the-loop system based on the hybrid technique to achieve dynamic ice-structure interaction in the ice basin. The main assumption behind the test setup is that, in order to model ice crushing against a vertically-sided structure, it is only necessary to model the part of the structure that is loaded by the ice. Since the mass of the section of an offshore structure loaded by sea ice is insignificant in comparison to the mass of the entire structure, this section can be modelled as a rigid, geometrical interface [21]. The response of the entire structure to the ice load is calculated using the equation of motion of the reference structure and the resulting structure response is imposed on the physical model by two electrical actuators [21]. Furthermore, it is assumed that the ice load on a structure remains unchanged whether ice drifts against a stationary structure or the structure moves through a stationary ice field.

Fig. 1a presents a detailed overview of the test setup. The test setup consisted of two aluminium plates which moved perpendicular to each other using two displacement-controlled electrical integrated motor actuators. Each actuator had a stroke of 0.2 m. An aluminium pile with a diameter of 200 mm was mounted at the centre of the bottom plate. The structure model, a downward-breaking ice cone with a slope angle of 60° and a waterline diameter of 300 mm, was bolted to the pile (Fig. 1b). The cone was made from polyamide 12 using selective laser sintering. The test setup was connected to a carriage that was attached to a bridge spanning the ice basin (Fig. 1c–d). The carriage moved the test setup through the ice field. The carriage was attached to the bridge via four dual bogies connected to twin rails. It was driven by a rack-and-pinion system with two drive pinions.

The bottom and the centre aluminium plates were instrumented with displacement sensors. The pile was instrumented with three load cells, which were located between the upper rim of the pile and the lower aluminium plate. The setup was instrumented with two additional but redundant S-type load cells mounted to the rods pushed by the linear actuators. In addition, the setup was instrumented with four accelerometers: one in the pile and one on each aluminium plate. The different sensors are described in detail in [20,25]. Lastly, two video cameras (GoPro Hero 9) were attached to the carriage to document ice-structure interaction in the ice-drift direction (Y-direction) and from the side (X-direction). Both cameras were located above the ice sheet and could therefore not sufficiently capture the downward ice-breaking process.

The setup used a micro-controller to control the displacement of the electric actuators. The control loop used the horizontal force of the ice on the physical structure model as an input and produced a structural displacement as an output. The horizontal force was calculated from the force measured using the three load cells located between the pile and the lowest plate, based on force and moment balances. The displacement was applied to the actuators using a PID controller.

The displacement of the electric actuators was calculated using the equations of motion of a reference structure. The equations of motion in the modal domain can be written in matrix form as

$$\ddot{w}_i(t) + 2\zeta_i\omega_i\dot{w}_i(t) + \omega_i^2 w_i(t) = \begin{bmatrix}\boldsymbol{\Phi}_{i,\mathrm{X;ice}} & \boldsymbol{\Phi}_{i,\mathrm{Y;ice}}\end{bmatrix}\begin{bmatrix}F_{i,\mathrm{X;ice}}(t)\\ F_{i,\mathrm{Y;ice}}(t)\end{bmatrix}. \tag{3}$$

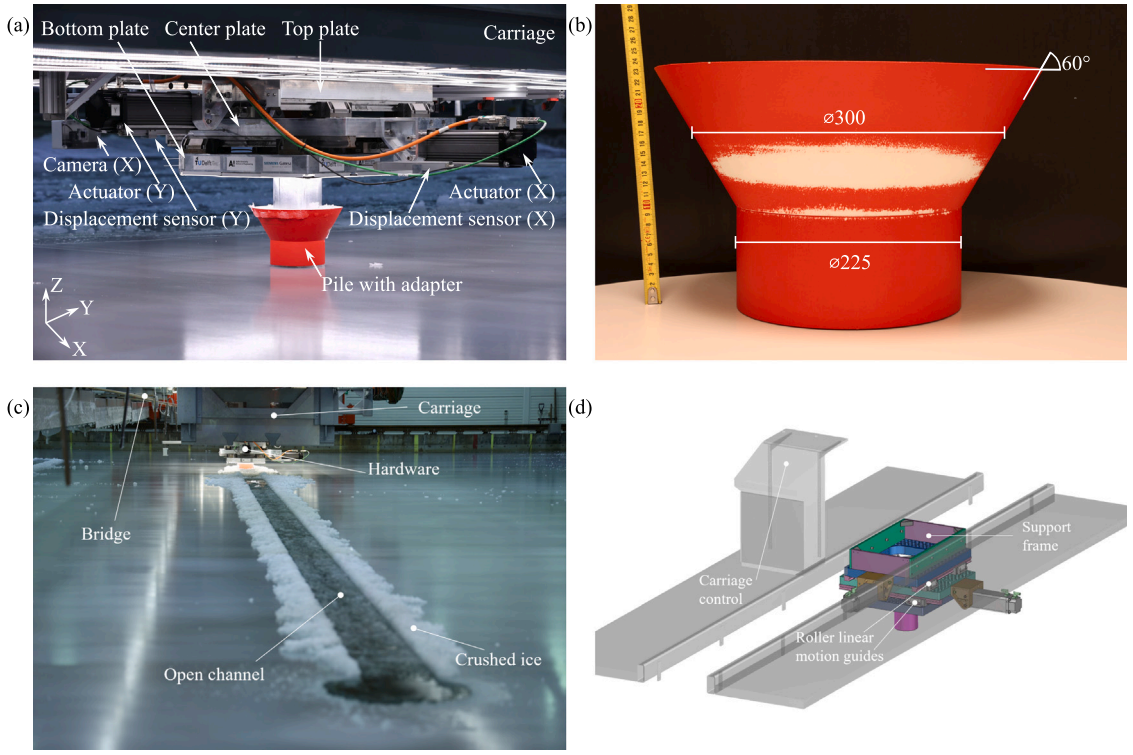

Fig. 1. (a) Detailed overview of the test setup. The ice drifted in the Y-direction. (b) Dimensions of the cone model. (c) General overview of the test setup in the ice and wave tank. (d) Overview of the test setup from within the carriage. Figures (c)–(d) are reproduced from [21], under the Creative Commons Attribution-NonCommercial-NoDerivatives 4.0 International License (http://creativecommons.org/licenses/by-nc-nd/4.0/).

In this equation, each mode i is described by its modal displacement $w_i(t)$ and its first and second derivatives with respect to time (indicated by the over-dots), its natural frequency ω_i, its critical damping ratio ζ_i and its mass-normalized mode shape values $\boldsymbol{\Phi}_{i,\mathrm{X;ice}}$ and $\boldsymbol{\Phi}_{i,\mathrm{Y;ice}}$ at the ice action point. The mass-normalized mode shape values $\boldsymbol{\Phi}_{i,\mathrm{X;ice}}$ and $\boldsymbol{\Phi}_{i,\mathrm{Y;ice}}$ satisfy the equation

$$\boldsymbol{\Phi}_{\mathbf{i}}^{\mathbf{T}} \cdot \mathbf{M} \cdot \boldsymbol{\Phi}_{\boldsymbol{i}} = \mathbf{1}\,, \tag{4}$$

where $\mathbf{M}$ represents the mass matrix and $\boldsymbol{\Phi}_{\boldsymbol{i}}$ represents the mass-normalized mode shape vector for mode i.

The displacement in the modal domain is solved in each iteration j using the semi-implicit Euler–Cromer method with a time step of $\Delta t = 1 \times 10^{-4}$ s as

$$\ddot{w}_i(t_j) = \begin{bmatrix}\boldsymbol{\Phi}_{i,\mathrm{X;ice}} & \boldsymbol{\Phi}_{i,\mathrm{Y;ice}}\end{bmatrix} \begin{bmatrix}F_{i,\mathrm{X;ice}}(t_j) \\ F_{i,\mathrm{Y;ice}}(t_j)\end{bmatrix} - 2\zeta_i\omega_i\dot{w}_i(t_j) + \omega_i^2 w_i(t_j) \tag{5}$$

$$\dot{w}_i(t_{j+1}) = \dot{w}_i(t_j) + \Delta t \cdot \ddot{w}_i(t_j) \tag{6}$$

$$w_i(t_{j+1}) = w_i(t_j) + \Delta t \cdot \dot{w}_i(t_{j+1})\,. \tag{7}$$

Before converting the displacement in the modal domain to the time domain, the displacement needs to compensate for a time delay τ of 4 ms to 5 ms between the output signal and the displacement measured using the displacement sensors. This delay can be compensated by calculating the displacement using the forward Euler method $w_{i;\mathrm{fp}}$ with a constant time delay $\Delta t_{\mathrm{fp}} = 5$ ms as

$$\dot{w}_{i;\mathrm{fp}}(t_j) = \dot{w}_i(t_j) + \Delta t_{\mathrm{fp}} \cdot \ddot{w}_{i;\mathrm{fp}}(t_j) \tag{8}$$

$$w_{i;\mathrm{fp}}(t_j) = w_i(t_j) + \Delta t_{\mathrm{fp}} \cdot \dot{w}_{i;\mathrm{fp}}(t_j)\,. \tag{9}$$

The displacement of the physical model at the ice action point at time $x(t_j)$ can be calculated as

$$x(t_j) = \sum_{i=1}^{n} \boldsymbol{\Phi}_{i,\mathrm{X;ice}} \cdot w_i(t_j) \tag{10}$$

$$y(t_j) = \sum_{i=1}^{n} \boldsymbol{\Phi}_{i,\mathrm{Y;ice}} \cdot w_i(t_j)\,. \tag{11}$$

Table 2
Test matrix for rigid and dynamic tests performed on April 25, 2023. The actual test distance for rigid tests with $v_d < 10\,\mathrm{mm\,s^{-1}}$ may have been shorter than 0.2 m.

Test type	Actuation device	Speed [$\mathrm{mm\,s^{-1}}$]	Distance [m]
Rigid	Setup	0.4	0.2
Rigid	Setup	0.6	0.2
Rigid	Setup	0.8	0.2
Rigid	Setup	1	0.2
Rigid	Setup	2	0.2
Rigid	Setup	4	0.2
Rigid	Setup	6	0.2
Rigid	Setup	8	0.2
Rigid	Carriage	10	0.4
Rigid	Carriage	20	0.8
Rigid	Carriage	40	0.8
Rigid	Carriage	60	1.2
Rigid	Carriage	80	1.6
Rigid	Carriage	100	2
Rigid	Carriage	200	2
Rigid	Carriage	500	3
Dynamic	Carriage	5	1
Dynamic	Carriage	15	3
Dynamic	Carriage	20	4
Dynamic	Carriage	30	6
Dynamic	Carriage	40	6
Dynamic	Carriage	70	3.5
Dynamic	Carriage	100	4

Although the numerical model outputs displacement in the X- and Y-direction, where the Y-direction coincides with the ice-drift direction, the results presented in this paper only focus on the displacements in the ice-drift direction.

2.3. Test matrix

Table 2 summarizes the test matrix. Two types of tests were performed. During the "rigid" tests, the ice cone moved through the ice sheet at constant ice-drift speeds. The test setup was considered rigid when no structural model was implemented in the numerical domain of the hybrid environment. Tests with an ice-drift speed $v_d < 10\,\mathrm{mm\,s^{-1}}$ used the actuator of the set up to move the structures, while in the remaining ones, the whole carriage was moved. Although Table 2 provides a prescribed distance for each test, the rigid tests were stopped prematurely once a circumferential crack occurred, as it was unlikely that the cone would meet the ice edge again within the remaining stroke of the actuator. During the "dynamic" tests, the hardware-in-the-loop functionality was used to model a compliant structure by implementing a structural model in the numerical domain of the hybrid environment.

During each experiment, the forces on the ice cone, the displacement of the actuator, and the displacement and speed of the carriage were recorded with a sampling frequency of 2000 Hz. The force and actuator displacement signals presented below are the raw signals. The signals of the carriage displacement and speed, as well as the derived relative velocity of the structure, were filtered using a 4th order Butterworth low-pass filter with a cut-off frequency of 30 Hz. Here, the relative velocity v_r is defined as:

$$v_r = v_d - \dot{y}, \tag{12}$$

where v_d is the carriage speed (ice-drift speed) and $\dot{y}$ is the structure velocity derived from the structure displacement y.

2.4. Structure model

The "dynamic" tests were performed with a linearized lumped-mass model of an idling 14 MW OWT on a monopile foundation located in the Baltic Sea. However, the main focus was on studying ice-structure interaction of a generic compliant conical structure in ice basin tests. Specific details of the reference structure are omitted in this paper to maintain the focus, but can be found in [2].

The structural properties of the OWT in the numerical model were scaled down to realize ice-structure interaction with the ice load levels typical for the basin. This was achieved using a scaling approach proposed in [20]. This approach assumes that the mean ice pressure on a vertical structure is preserved at full-scale and at model-scale (in the ice basin). The scaling factor λ_F is defined as the ratio of the mean crushing load at model-scale $\bar{F}_m$ to mean crushing load at prototype-scale $\bar{F}_p$,

$$\lambda_F = \frac{\bar{F}_m}{\bar{F}_p}. \tag{13}$$

The mean crushing load at model-scale $\bar{F}_m$ is defined as the mean measured horizontal load on a vertical structure at an ice-drift speed of $100\,\mathrm{mm\,s^{-1}}$ over a distance of 1.5 m. The prototype-scale mean load $\bar{F}_p$ can be defined based on measurements, design

Table 3
Physical quantities scaled using scale factor λ_F. Table adapted from Hammer et al. [2].

Physical quantity	Unit	Scale factor
Time	s	1
Structural displacement	m	1
ice-drift speed	$m\,s^{-1}$	1
Frequency	Hz	1
Mass	kg	λ_F
Stiffness	$N\,m^{-1}$	λ_F
Damping	$N\,s\,m^{-1}$	λ_F
Damping ratio	–	1
Mass-normalized mode shape	$kg^{-0.5}$	$\lambda_F^{-0.5}$
Mean (brittle crushing) load	N	λ_F

guidelines, or simulation results. The scaling factor affects the properties of the structure, namely its mass and its damping and stiffness coefficients, while the kinematics remain at the prototype-scale. A summary of the scaling factors is presented in Table 3.

Considering that the experiments in this study were performed using a conical structure, the mean horizontal force $\bar{F}_m$ is not representative of brittle crushing. Instead, scaling represents choosing a sensitivity factor that scales the structural properties to achieve ice-structure interaction. The final scaling factor was $\lambda_F = 1856$. The scaled values for ω_i, ζ_i, and $\boldsymbol{\Phi}_i$ are presented in the Appendix (Table A.2). The model is truncated to include the lowest natural frequencies up to 20 Hz to reduce computational complexity. Moreover, natural frequencies above 20 Hz are unlikely to be excited by ice loads [26].

Nonetheless, the dimensions of the structural model, the tested ice-drift speeds, and the flexural strength of the model ice were representative of navigational aids, such as the Pietarinkanta channel marker in the Gulf of Bothnia [27], scaled using Cauchy–Froude strength scaling with a scaling factor of 2 to 4. However, this only applies to the rigid tests.

2.5. Measurement uncertainty

The placement of the load cells between the pile rim and the bottom plate introduced a non-linear error when measuring the horizontal force F_Y. The experimental results are insightful nonetheless when analysed qualitatively. Most importantly, this error did not affect the frequency response of the structure in dynamic tests.

The test setup was originally designed to measure ice loads on vertical structures based on the assumption that vertical forces F_Z were negligible and that the vertical location of the ice-structure contact point remained constant. These assumptions do not hold in tests with conical structures. As a result, the load cells were positioned in a statically indeterminate configuration, which introduced F_Z-dependent error in F_Y.

The measurement error in the pile load cells $F_{Y,\text{pile}}$ can be estimated based on results from rigid tests with ice drift speeds $v_d \geq 10\,\text{mm}\,\text{s}^{-1}$. The measurement error e_{mes} is defined as:

$$e_{\text{mes}} = 100 \times \left| \frac{F_{Y,\text{pile}} - F_{\text{actuator}}}{F_{\text{actuator}}} \right|, \tag{14}$$

where F_{actuator} is measured using the Y-actuator load cell. To reduce differences in force measurements due to noise, the measurement error was calculated using force percentiles. At the 95th percentile, the error was $1.2\% < e_{\text{mes}} < 11.9\%$ and it decreased below 10% at the 66th percentile ($2.3\% < e_{\text{mes}} < 9.6\%$). It should be pointed out that F_{actuator} also measured the inertia of the test setup. This possibly introduced additional uncertainty in the error estimate.

Rigid tests at $v_d < 10\,\text{mm}\,\text{s}^{-1}$ were executed using the Y-actuator. This introduced a different v_d-dependent error in F_{actuator}, which made the above-defined e_{mes} unreliable. However, since the error in $F_{Y,\text{pile}}$ was dependent on F_Z and the 95th percentile of F_Z for $v_d < 10\,\text{mm}\,\text{s}^{-1}$ was smaller than the 95th percentile of F_Z for $v_d \geq 10\,\text{mm}\,\text{s}^{-1}$, e_{mes} was assumed to be within the same range.

3. Results and analysis

3.1. Rigid tests

Two different ice failure modes were observed (Figs. 2, 3): local failure of the ice edge and bending failure. Local failure of the ice edge occurred at low ice-drift speeds. The force–displacement signals resembled a sawtooth wave with a convex load build-up followed by a sudden force drop (Fig. 2). The mean and standard deviation of the driving distance between two consecutive load drops were $8\,\text{mm} \pm 5\,\text{mm}$. The distances were independent of ice drift speed, similar to local spalling or flaking failure of ice [28]. At $v_d \geq 6\,\text{mm}\,\text{s}^{-1}$, the sawtooth wave had superimposed stochastic force fluctuations. At $v_d \geq 10\,\text{mm}\,\text{s}^{-1}$ (Fig. 3), the force–displacement signals resembled a stochastic signal with a positive non-zero mean. These load fluctuations are characteristic of brittle crushing failure [29].

Local failure of the ice edge could not be observed directly during testing. The ice sheet deflected downward when the cone indented the ice edge, and water flooded the ice. At low ice-drift speeds, the ice sheet repeatedly bounced up, but the ice remained flooded. At $v_d = 8\,\text{mm}\,\text{s}^{-1}$, the ice edge in front of the cone appeared to have the same shape as the cone (Fig. 4), suggesting that

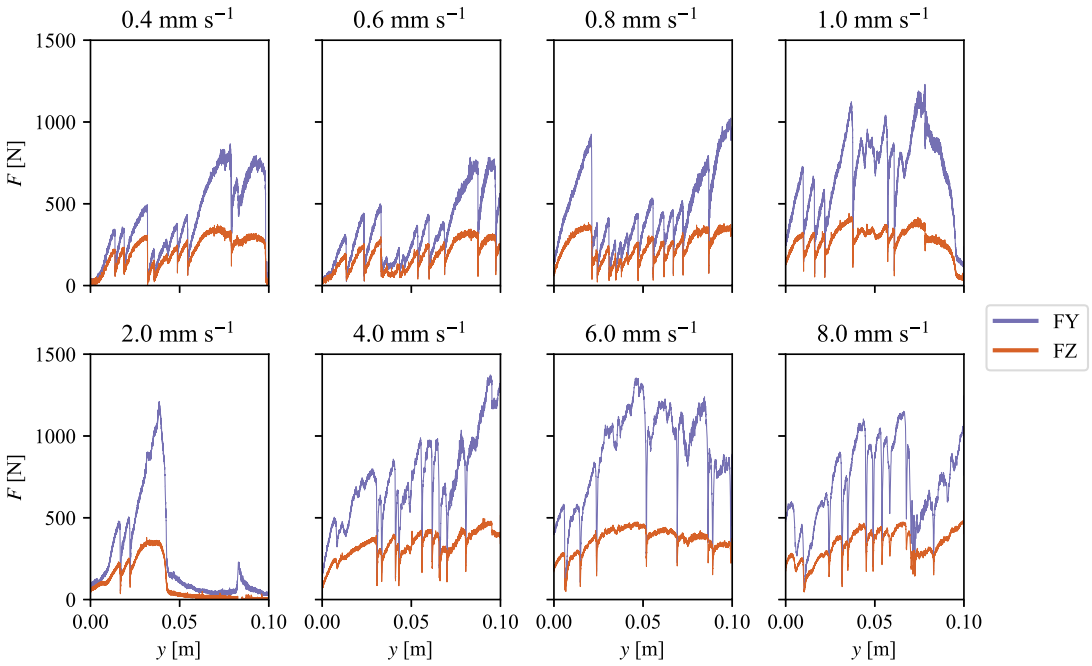

Fig. 2. Force–displacement (F–y) histories of the rigid tests with $v_d < 10\,\mathrm{mm\,s^{-1}}$. Each plot shows the first 0.1 m of the driving distance regardless of test length.

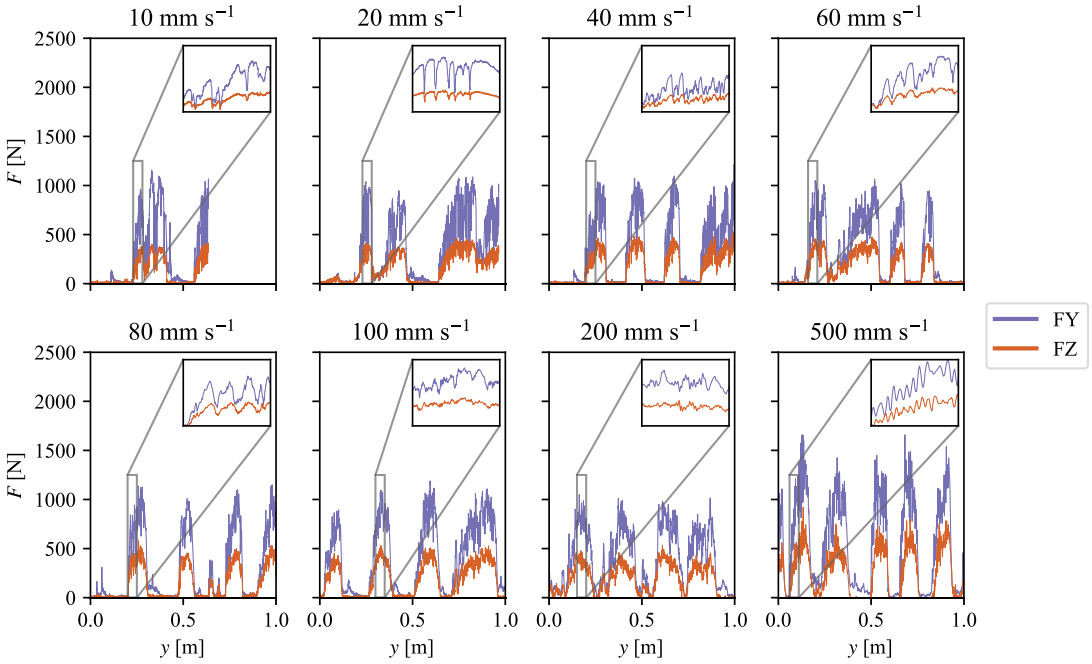

Fig. 3. Force–displacement (F–y) histories of the rigid tests with $v_d \geq 10\,\mathrm{mm\,s^{-1}}$. Each plot shows an extract equivalent to an ice-drift distance $y = 1$ m regardless of test length. The highlighted sections in each plot all have the same axis limits.

local failure occurred over a wide contact area. It was not possible to visually inspect the ice edge in front of the cone at any other instances. The edges of the channel behind the cone remained deformed and flooded. Furthermore, differently sized ice fragments floated behind the cone, including large ice wedges from bending failure events and small ice pieces from local failure events. The small ice pieces also floated in front of the cone when the ice sheet was submerged.

Although it was not possible to determine the local failure mode, the force–displacement signals and indirect visual observations suggest that the ice experienced shear and crushing failure. In the force–displacement signals (Fig. 2), sawtooth waves were

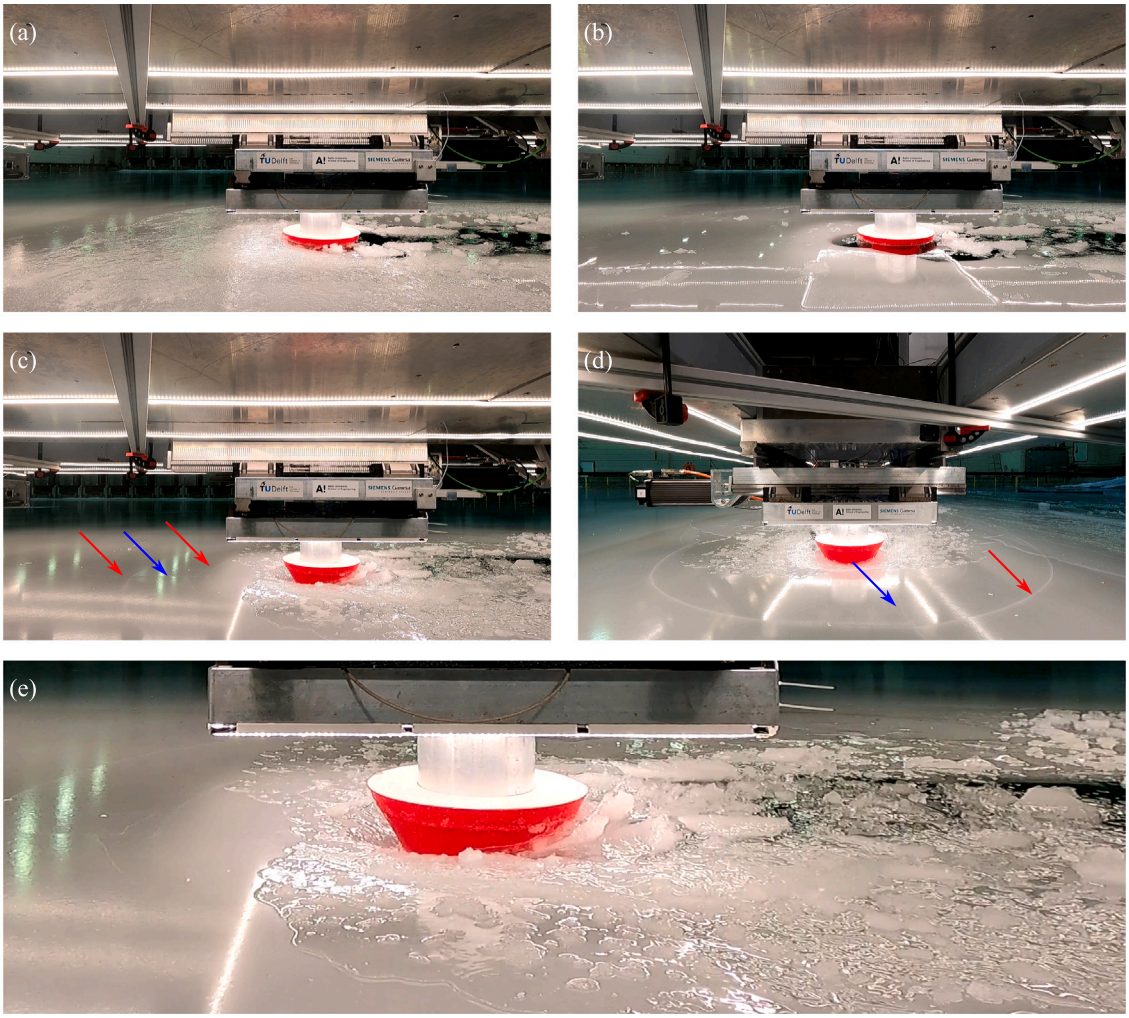

Fig. 4. Still frames from different rigid tests: (a) Ice sheet before the rigid test at $v_d = 8\,\mathrm{mm\,s^{-1}}$. (b) Ice sheet at the end of the rigid test at $v_d = 8\,\mathrm{mm\,s^{-1}}$. The carriage moved away from the ice edge before this still frame was taken. (c–e): Scenes from the rigid test at $v_d = 200\,\mathrm{mm\,s^{-1}}$. (e) Shows a cropped close-up of (c) to highlight the ice fragments around the cone. Both radial (blue) and circumferential (red) cracks were visible. Note that the draft of the cone remained constant throughout the rigid tests. The draft appears to change in photos (a)–(d) due to the downward deflection of the ice sheet. At $v_d = 200\,\mathrm{mm\,s^{-1}}$, the interaction between the ice and the structure occurs so quickly that the water does not have sufficient time to flood the ice sheet before bending failure occurs. This visually exaggerates the perceived draft of the cone.

interpreted as "shear failure", while stochastic force fluctuations were interpreted as "crushing failure". This interpretation is subjective and the identified failure mode will be referred to as local failure of the ice edge.

Bending failure was observed at ice-drift speeds above $v_d \geq 10\,\mathrm{mm\,s^{-1}}$ because these tests were performed over longer distances (Fig. 3). During each bending failure event, the mean force initially increased and then plateaued before decreasing. The force fluctuations during the plateaus were the result of local failure of the ice edge. At higher ice-drift speeds, e.g., at $v_d \geq 200\,\mathrm{mm\,s^{-1}}$, radial and evenly-spaced circumferential cracks were visible in front of the cone (Fig. 4) because the high ice-drift speed limited the extent of flooding. The mean bending failure length L_b, estimated as the distance between two consecutive load increases, varied between $0.1\,\mathrm{m} \leq L_b \leq 0.3\,\mathrm{m}$ and decreased with increasing ice-drift speed (Fig. 5). Overall, L_b was 3–15 times shorter than the calculated characteristic lengths $l_{c,beam}$ and $l_{c,plate}$ (Eq. (1)).

3.2. Dynamic tests

In the dynamic tests, the ice failed in the same two ice failure modes as in the rigid tests: local failure of the ice edge and bending failure. Structural displacements associated with local failure were visible at low ice-drift velocities during periods of low relative velocity v_r, e.g., at $v_d = 5\,\mathrm{mm\,s^{-1}}$ (Fig. 6a). Local failure caused the structure model to accelerate after each force drop,

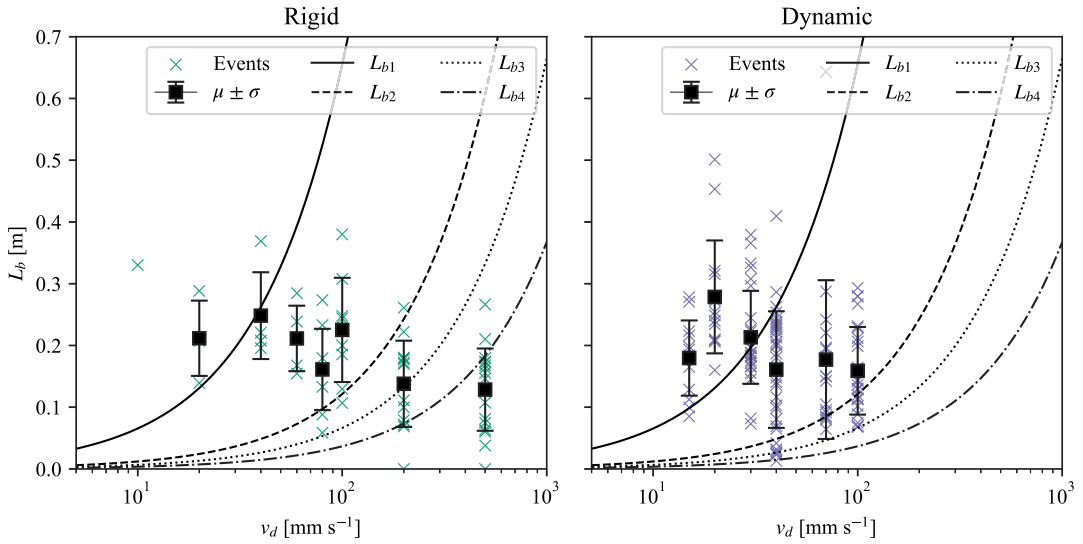

Fig. 5. Scatter plot of the estimated bending failure length (L_b) against the ice-drift speed (v_d) for rigid and dynamic tests including the mean (μ) and the standard deviation (σ). L_b is defined as the distance between two load increases associated with bending failure. The theoretical bending failure lengths are calculated using Eq. (15) for the 1st–4th natural frequencies ($L_{b1} - L_{b4}$) of the structure model.

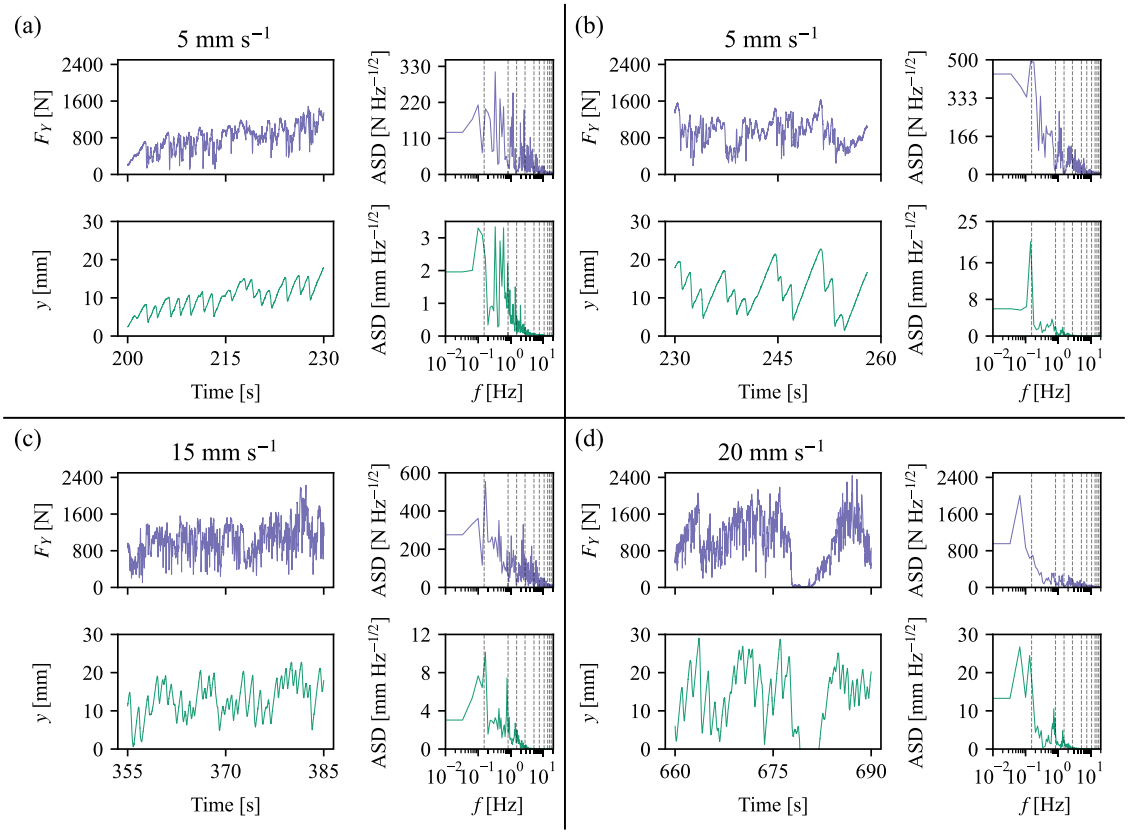

Fig. 6. Force (F) and displacement (y) histories and the corresponding amplitude spectral densities (ASDs) of different dynamic tests at different ice-drift speeds: (a–b) $v_d = 5\,\mathrm{mm\,s^{-1}}$, (c) $v_d = 15\,\mathrm{mm\,s^{-1}}$, and (d) $v_d = 20\,\mathrm{mm\,s^{-1}}$. The dashed vertical lines in the ASDs indicate the natural frequencies of the numerical structure mode. The full force–displacement–relative velocity histories can be found in the Appendix (Figs. A.1, A.2, A.3). Note the different y-axis limits for each ASD.

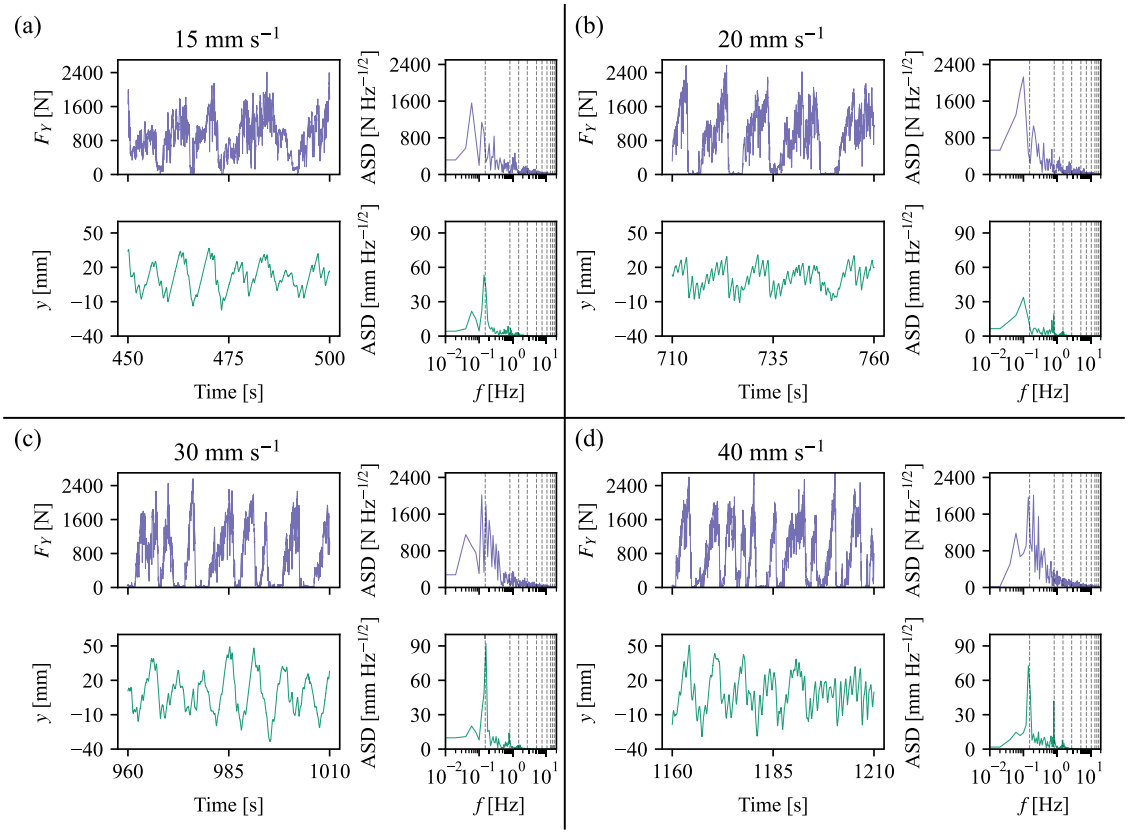

Fig. 7. Force (F) and displacement (y) histories and the corresponding amplitude spectral densities (ASDs) of different dynamic tests at different ice-drift speeds: (a) $v_d = 15\,\mathrm{mm\,s^{-1}}$, (b) at $v_d = 20\,\mathrm{mm\,s^{-1}}$, (c) at $v_d = 30\,\mathrm{mm\,s^{-1}}$ and (d) $v_d = 40\,\mathrm{mm\,s^{-1}}$. The dashed vertical lines in the ASDs indicate the natural frequencies of the numerical structure mode. The full force–displacement–relative velocity histories can be found in the Appendix (Figs. A.2, A.3, A.4, A.5).

resulting in a sawtooth displacement–time signal. The force drops occurred regularly at a frequency between the 1st and 2nd natural frequencies of the structure model. The force drops and the corresponding displacements y were periodic enough to be captured in the respective amplitude spectral density (ASD). When local failure did not occur (Fig. 6b), the force and displacement time-series showed characteristics of multi-modal interaction with an amplified response of the 1st mode [2].

Local failure was also observed momentarily in dynamic tests at $v_d = 15\,\mathrm{mm\,s^{-1}}$ and $v_d = 20\,\mathrm{mm\,s^{-1}}$ (Fig. 6c–d). The failure frequencies associated with local failure were around 2 Hz (between the 3rd and 4th natural frequencies of the structure). In both cases, the displacement ASD showed that the 3rd natural frequency of the structure model was excited. However, the corresponding peak had low prominence. A different type of local ice failure was observed at $v_d = 70\,\mathrm{mm\,s^{-1}}$ (Fig. A.6). The force signal consisted of random load fluctuations around a mean force, resembling crushing failure. The structure seemed to oscillate at the 2nd and 3rd natural frequencies independent of the load signal.

Quasi-periodic structural vibrations were observed in tests with $15\,\mathrm{mm\,s^{-1}} \leq v_d \leq 100\,\mathrm{mm\,s^{-1}}$. The ice failed periodically through bending failure at failure frequencies close to the 1st (Fig. 7) and 2nd (Fig. 8) natural frequencies of the structure model. The displacement ASD for each test showed that the structure model was simultaneously excited at multiple frequencies. In some tests, e.g., $v_d = 15\,\mathrm{mm\,s^{-1}}$, $v_d = 30\,\mathrm{mm\,s^{-1}}$, and $v_d = 100\,\mathrm{mm\,s^{-1}}$, one frequency dominated the structural response. In other tests, i.e. $v_d = 20\,\mathrm{mm\,s^{-1}}$, $v_d = 40\,\mathrm{mm\,s^{-1}}$, and $v_d = 70\,\mathrm{mm\,s^{-1}}$ the displacement ASD contained two prominent peaks. The displacement ASD of the tests at $v_d = 20\,\mathrm{mm\,s^{-1}}$ and $v_d = 40\,\mathrm{mm\,s^{-1}}$ showed sustained free oscillations at the 2nd natural frequency.

Fig. 9 presents still frames from the dynamic tests at $v_d = 5\,\mathrm{mm\,s^{-1}}$, $v_d = 40\,\mathrm{mm\,s^{-1}}$, and $v_d = 100\,\mathrm{mm\,s^{-1}}$. Similar to the rigid tests, local failure of the ice edge could not be observed directly during the dynamic tests. At $v_d = 5\,\mathrm{mm\,s^{-1}}$, the cone appeared to remain in contact with the ice edge and the ice sheet in front of the cone was submerged. However, the structure repeatedly moved towards the ice edge, suggesting some ice had failed locally. At $v_d = 40\,\mathrm{mm\,s^{-1}}$ and $v_d = 100\,\mathrm{mm\,s^{-1}}$, the ice failed through bending failure. The visibility of each bending failure event depended on the degree of flooding in front of the cone. For example, it was possible to observe an ice wedge submerging after a bending failure event at $v_d = 40\,\mathrm{mm\,s^{-1}}$ (Fig. 9). At the same time, it was not possible to observe radial or circumferential cracks before the failure event. At $v_d = 100\,\mathrm{mm\,s^{-1}}$, the high ice-drift speed prevented extensive flooding, which made it possible to observe circumferential and radial cracks in front of the cone. Lastly, similar to the rigid tests, the channel behind the cone showed that the ice remained deformed after the cone passed. Differently sized ice fragments in the channel and around the cone indicated that the ice failed through bending failure and local failure.

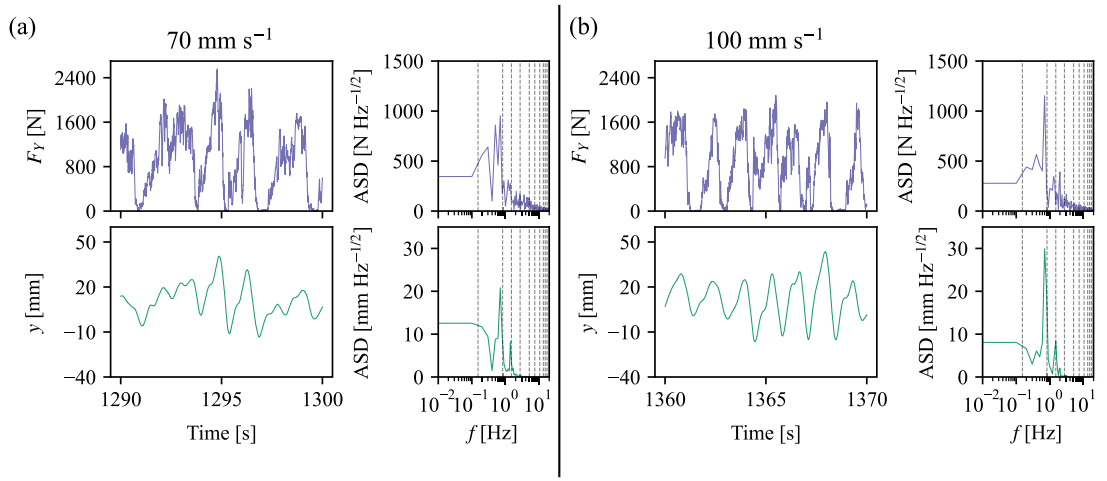

Fig. 8. Force (F_Y) and displacement (y) histories and the corresponding amplitude spectral densities (ASDs) of different dynamic tests at different ice-drift speeds: (a) $v_d = 70\,\mathrm{mm\,s^{-1}}$, (b) $v_d = 100\,\mathrm{mm\,s^{-1}}$ The dashed vertical lines in the ASDs indicate the natural frequencies of the numerical structure mode. The full force–displacement–relative velocity histories can be found in the Appendix (Figs. A.6, A.7).

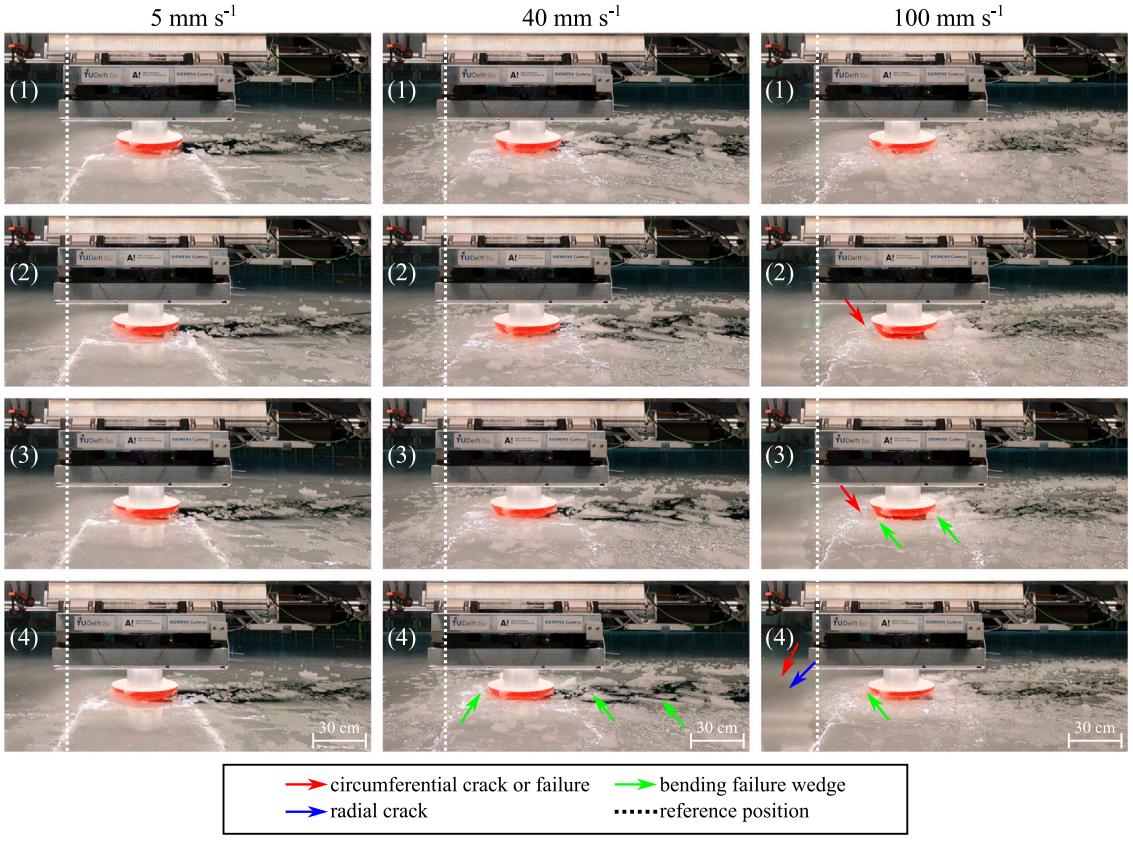

Fig. 9. Still frames from different dynamic tests at ice-drift speeds $v_d = 5\,\mathrm{mm\,s^{-1}}$ (left), $v_d = 40\,\mathrm{mm\,s^{-1}}$ (centre), and $v_d = 100\,\mathrm{mm\,s^{-1}}$ (right). For each column, photos (1)–(4) occur chronologically but at irregular time intervals. The dashed white line is a visual reference which highlights the initial position of the left-most edge of the test setup based on photo (1).

Similarly to the rigid tests, the mean L_b varied between $0.1\,\mathrm{mm\,s^{-1}}$ to $0.3\,\mathrm{mm\,s^{-1}}$. To analyse the L_b further, L_b can be compared to the theoretical L_b needed for the bending failure frequency to coincide with a natural frequency of the structure model. The theoretical L_b can be calculated as

$$L_b = v_d / f_b\,, \tag{15}$$

where f_b is the bending failure frequency [8]. The theoretical bending failure lengths corresponding to the 1st to the 4th natural frequencies of the structure model, $L_{b1} - L_{b4}$, are presented in Fig. 5 along with the estimated L_b. The estimated L_b coincide with the theoretical L_{b1} at $v_d = 15\,\mathrm{mm\,s^{-1}}$ and $v_d = 20\,\mathrm{mm\,s^{-1}}$ to $30\,\mathrm{mm\,s^{-1}}$, and with $L_{b2} - L_{b3}$ at $v_d = 40\,\mathrm{mm\,s^{-1}}$ to $100\,\mathrm{mm\,s^{-1}}$. Furthermore, the amplitude of the displacement oscillations increased when f_b matched a natural frequency of the structure model (Fig. 10a). The largest oscillations were observed at $v_d = 30\,\mathrm{mm\,s^{-1}}$ and $v_d = 40\,\mathrm{mm\,s^{-1}}$ when f_b matched the 1st natural frequency of the structure. At $v_d = 5\,\mathrm{mm\,s^{-1}}$, the displacement measurements had the smallest spread because the ice failed predominantly locally.

Lastly, Fig. 10b shows that the structure experienced two types of ice-structure interaction depending on v_d. At $v_d \leq 40\,\mathrm{mm\,s^{-1}}$, the maximum kernel density estimate was around $v_r = 0\,\mathrm{mm\,s^{-1}}$. A v_r near $0\,\mathrm{mm\,s^{-1}}$ indicated that the structure velocity $\dot{y}$ was equal and opposite of v_d, and that structure remained in contact with the ice. At $v_d = 70\,\mathrm{mm\,s^{-1}}$ and $v_d = 100\,\mathrm{mm\,s^{-1}}$, the maximum kernel densities were located around $v_r = 50\,\mathrm{mm\,s^{-1}}$ and $v_r = 100\,\mathrm{mm\,s^{-1}}$, respectively. At these ice drift speeds, the structure no longer maintained contact with the ice edge.

3.3. Comparison

The same failure modes were observed in the rigid and dynamic tests: local failure of the ice edge and bending failure. The force signature of local failure of the ice edge was determined to present small amplitude sawtooth waves with significant load drops on top of an increasing mean force (Figs. 2, 6). In the rigid tests, the sawtooth waves were regular enough to estimate the distance between consecutive load drops. As the ice-drift speed increased, the sawtooth waves became more irregular. In the dynamic tests, the sawtooth waves were less regular, and it was not possible to estimate the distance between consecutive load drops. Moreover, local failure occurred over longer distances during the dynamic tests.

The main difference between local failure in rigid and dynamic tests was the ice-drift speed at which local failure could occur. During the dynamic tests, local failure was observed at ice-drift speeds up to $v_d = 40\,\mathrm{mm\,s^{-1}}$ because the relative velocity between the structure model and the ice was low (Fig. 10). As a result, local failure could occur at higher ice-drift speeds in the dynamic tests.

Ice-structure interaction with the compliant structure model also seemed to affected the bending failure length. Overall, the mean bending failure lengths in rigid and dynamic tests fell within the same range (Fig. 5). In the dynamic tests, more bending failure length estimates coincided with the theoretical bending failure lengths needed to match a natural frequency of the structure model. This suggests that the structure model affected the bending failure length of the ice.

4. Discussion

Two types of ice-induced vibrations were observed during the experiments: local failure-induced vibrations and bending failure-induced vibrations. Although it was not possible to determine the local failure mode, the force–displacement signals (Fig. 2) and indirect visual observations suggest that the ice experienced shear and crushing failure. Literature on shear failure against conical or inclined structures is sparse. Neill reported that ice failed in bending or shear against inclined piles and piers with a high inclination angle [30]. Xu et al. reported that shear and crushing failure occurred during most interaction processes with cones and delayed the occurrence of the peak load at bending failure [18]. Määttänen described the shear failure of the ice edge as a failure mechanism competing with bending failure [31], and he hypothesized that repeated shear failure may have been the origin of sustained vibrations on a navigational aid in the Baltic Sea [27]. The results presented in this study (Fig. 3) agree with the observations by Xu et al. [18] and Määttänen [31] and support the possibility of local failure-induced vibrations on channel markers [27].

To the knowledge of the authors, there are no publications discussing the local failure of the ice edge against conical structures in model-scale experiments. Nevertheless, ice-induced vibrations as a result of repeated shear failure were observed in ice basin tests (which did not consider scaling) using compliant inclined plates and faceted cones in thick columnar saline ice [32] and columnar freshwater ice [33,34]. The force signals associated with shear failure were characterized by repeated sawtooth waves. However, the underlying failure mechanism was fundamentally different because the columnar ice failed in shear along the grain boundaries. Recent ice basin tests with an upward-breaking cone tested in three different ice sheets with varying strength showed that higher-strength model ice experienced local failure before bending failure, while lower-strength model ice failed purely in bending [35]. It is possible that local failure against conical structures has not been reported before in the context of model-scale ice basin tests because model ice with a flexural strength between 30 kPa to 50 kPa could not model local failure. It should be investigated if a strength limit exists below which model ice cannot reproduce the failure modes expected in full-scale ice-structure interaction or known effects which affect ice-structure interaction, such as the pressure–area effect.

Bending failure-induced vibrations occurred at critical ice-drift speeds where the bending failure frequency coincided with the 1st ($30\,\mathrm{mm\,s^{-1}}$ to $40\,\mathrm{mm\,s^{-1}}$) and 2nd ($70\,\mathrm{mm\,s^{-1}}$ to $100\,\mathrm{mm\,s^{-1}}$) natural frequencies of the structure model. At ice-drift speeds where the bending failure frequency was not close to a natural frequency of the structure, the displacement response of the cone was a superposition of a quasi-static response to the ice load and free oscillations at higher natural frequencies, consistent with observations by [16]. The force signals from the rigid and dynamic tests of the current study were similar to the force signals recorded on the JZ20-2 MUQ platform in the Bohai Sea [8]. The current study achieved more representative ice-structure interaction as a result of repeated bending failure compared to existing model-scale ice basin studies [7,15,16,36]. In previous studies, the ice failed through a two-time bending failure process. This two-time bending failure is not commonly described in field observations [18,19] and was likely caused by the low strength of the Cauchy–Froude scaled model ice [36]. Moreover, since the scaling laws employed

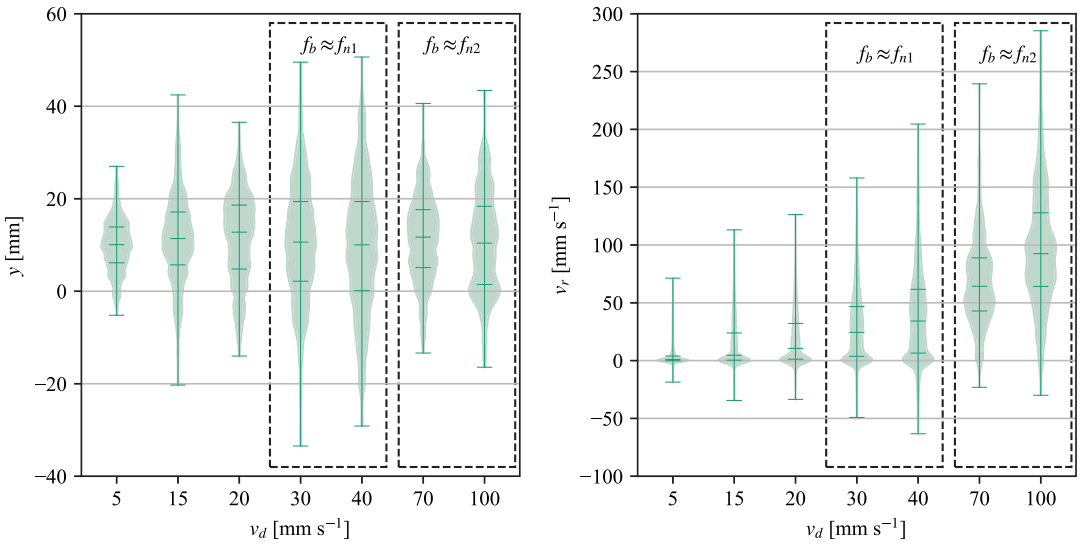

Fig. 10. (a) Violin plot of the structural displacement y and (b) violin plot of the relative velocity v_r for each ice-drift speed v_d. The horizontal lines indicate the global minimum and maximum values, as well as the 25th, 50th and 75th percentile. The violin plots were made using Scott's rules of thumb for bandwidth estimation and a Gaussian kernel.

in the current study did not scale the ice drift speed (in contrast to Cauchy–Froude scaling), the current study (Fig. 5) avoided velocity-dependent changes in the bending failure length observed at high ice drift speeds [16]. One possible explanation for the reduced bending failure length at higher ice-drift speeds is hydrodynamic resistance leading to an effective increase in the stiffness of the ice sheet, which in turn can affect the bending failure length [37]. Cauchy–Froude scaling does not account for these non-linear effects. It is important to note that the bending failure lengths reported in this study (Fig. 5) were estimated indirectly using force–displacement signals instead of being measured directly. Future studies should consider measuring the sizes of the ice blocks formed during ice-structure interaction, enabling a more thorough analysis of the bending failure lengths and the stress states that led to their formation [38,39].

Choosing the right model ice and an appropriate set of scaling laws is paramount to studying ice-structure interaction with a hardware-in-the-loop test setup because the test setup uses the force signal to prescribe a displacement to the physical indenter. The test setup cannot distinguish between force signals associated with different failure modes, e.g., bending failure and local failure. It is therefore important to use model ice which models all of the expected failure processes on the full-scale reference structure. Most model-scale experiments studying ice-cone interaction used Cauchy–Froude scaling to scale the reference structure and the ice strength [7,16,36]. In practice, only selected ice properties, e.g., the thickness and the flexural strength, are scaled with the scaling factor, whereas the remaining properties depend on the model ice. Model ice may not maintain the same ratios between different mechanical properties across different scaling factors, nor may it fail in the same failure modes [35,40,41]. The current experiments were performed using "cold" model ice. This ice has been used successfully in model-scale experiments investigating ice-induced vibrations on vertically sided structures [2,22] because it has a similar transition speed as sea ice, exhibits a velocity effect, and fails in crushing [20]. However, further research is needed to investigate if this model ice models other failure modes, such as bending failure, correctly. The lack of secondary bending failure seems promising. Ultimately, the validity of scaled ice basin tests can only be determined using high-resolution full-scale reference data. This data could be collected by systematically instrumenting offshore structures with force and acceleration measurement devices and by monitoring sea ice dynamics in the vicinity of offshore structures using seismometers, tiltmeters and strainmeters. The latter method has been tested in level ice and ridge conditions [42,43] and could also offer valuable information about the ice conditions and the stress states of the ice around offshore structures.

5. Conclusion

This paper explored ice-structure interaction between drifting level ice and a compliant conical structure through ice basin tests with a downward-breaking cone and a hardware-in-the-loop system based on the hybrid technique. Two types of experiments were performed: dynamic tests performed with a structure model of an offshore wind turbine (OWT) implemented in the numerical domain of the hybrid environment, and rigid tests without any implementation of a structure model. The structure model was scaled to facilitate ice-structure interaction in the ice basin rather than to represent the structural dynamics of an OWT.

In both types of tests, the ice exhibited the same two failure modes: (1) local failure of the ice edge and (2) bending failure. The main results from the rigid tests were the following:

- At low ice-drift speeds, the ice edge failed periodically against the cone prior to the formation of a circumferential crack. The corresponding force–time histories displayed characteristics of both crushing and shear failure.

- At higher ice-drift speeds, the ice failed in bending. The bending failure process differed from previous experiments because the resulting wedges did not fail a second time against the structure.

The main results from the dynamic tests were the following:

- Both local failure and bending failure can lead to high-amplitude periodic structural vibrations.
- Ice-induced vibrations as a result of bending failure were observed at the 1st and 2nd natural frequencies of the structure model. The bending failure frequency depended on the ice-drift speed.

These results were unexpected for two reasons: (1) local failure of the ice edge has not been reported in the context of ice basin tests with conical structures and (2) local failure can lead to ice-induced vibrations.

Although this study performed ice basin tests without a reference full-scale structure, the main findings offer valuable insight into ice-structure interaction with conical structures. The results confirm historical observations that bending failure-induced vibrations can occur at critical ice-drift speeds [8,9]. These critical ice-drift speeds can be identified from the natural frequencies of a structure. Moreover, these experiments show that local failure-induced vibrations can occur at low interaction speeds. This result supports the hypothesis that compliant structures may experience sustained vibrations due to repeated shear failure of the ice edge [27]. The low interaction speed needed for local failure can be the result of low ice-drift speed or low relative velocity between the ice and the structure. Local failure-induced vibrations may thus introduce an additional vibration regime to consider in the structural design of conical offshore structures.

Lastly, the findings of this study provide new insight into ice basin tests focused on ice-structure interaction with conical structures. The current results were achieved with a novel test setup, which made it possible to study multi-modal structural vibrations, and a novel model ice, which led to more representative bending failure. The observed ice-induced vibrations have not been obtained in previous model-scale experiments, which applied Cauchy–Froude strength scaling to the ice and the structure model. The results provide a new perspective on scaling of dynamic model-scale experiments with conical structures; scaling should focus on modelling the expected ice failure modes correctly. Future experiments will focus on exploring new scaling relationships for dynamic ice-structure interaction with an ice cone.

CRediT authorship contribution statement

Alice Petry: Writing – review & editing, Writing – original draft, Visualization, Software, Project administration, Methodology, Investigation, Formal analysis, Data curation, Conceptualization. **Otto Puolakka:** Writing – review & editing, Resources, Project administration, Methodology, Investigation, Data curation, Conceptualization. **Tim C. Hammer:** Writing – review & editing, Software, Project administration, Methodology, Investigation, Data curation, Conceptualization. **Hayo Hendrikse:** Writing – review & editing, Writing – original draft, Supervision, Software, Resources, Project administration, Methodology, Investigation, Funding acquisition, Data curation, Conceptualization. **Arttu Polojärvi:** Writing – review & editing, Writing – original draft, Supervision, Resources, Project administration, Methodology, Investigation, Funding acquisition, Conceptualization.

Declaration of Generative AI and AI-assisted technologies in the writing process

During the preparation of this work A. Petry used Grammarly, ChatGPT-3.5 and ChatGPT-4o (free tier) in order to improve readability. After using this tool/service, the authors reviewed and edited the content as needed and take full responsibility for the content of the published article.

Declaration of competing interest

The authors declare that they have no known competing financial interests or personal relationships that could have appeared to influence the work reported in this paper.

Acknowledgements

Funding from the European Union–NextGenerationEU instrument through Research Council of Finland under grant number (348586) *WindySea — Modelling engine to design, assess environmental impacts, and operate wind farms for ice-covered waters* is acknowledged. The authors would like to thank Laura van Dijke, Cody C. Owen, Kees van Beek and Jeroen Koning from Delft University of Technology, Jeffrey Hoek and Tom Willems from Siemens Gamesa Renewable Energy, and Teemu Päivärinta and Lasse Turja from Aalto Ice and Wave Tank for their help and assistance before, during, and after the test campaign. The authors would also like to thank Cody C. Owen and Vegard Hornnes for proofreading the manuscript. A. Petry would also like to thank Mikko Suominen, Malith Prasanna, Jukka Tuhkuri, Knut Høyland and Wenjun Lu for interesting and fruitful discussions. H. Hendrikse would like to express gratitude to the contributing organizations of the SHIVER project: TU Delft, Siemens Gamesa Renewable Energy, and the Dutch Ministry of Economic Affairs and Climate Policy through the 'Toeslag voor Topconsortia voor Kennis en Innovatie (TKI's)' initiative.

Appendix

See Figs. A.1–A.7 and Tables A.1–A.2.

Table A.1
Ice thickness measurements (h) at different positions along the test tracks for the rigid and dynamic tests.

Test	Position [m]	h [mm]
Rigid	21	30
	18	29
	15	27
	12	28
	9	28
	6	32
	3	30
Dynamic	32	27
	28	29
	24	29
	20	29
	16	30
	12	28
	8	29
	4	29
	0	30
	Extra	31

Table A.2
Properties of the scaled structure model of an idling offshore wind turbine at the ice action point: the natural frequency f_n, the critical damping ratio ζ and the mass-normalized mode shape values $\boldsymbol{\Phi}_{i,\mathrm{X;ice}}$ and $\boldsymbol{\Phi}_{i,\mathrm{Y;ice}}$ at the ice action point.

Mode	f_n Hz	ζ %	$\boldsymbol{\Phi}_{\mathrm{X;ice}}$ $10^{-3}\mathrm{kg}^{-0.5}$	$\boldsymbol{\Phi}_{\mathrm{Y;ice}}$ $10^{-3}\mathrm{kg}^{-0.5}$
0	0.153	0.8	0	−1.94
1	0.154	0.8	1.96	0
2	0.824	1.2	0	13.23
3	0.888	1.3	−15.46	0
4	1.504	2.6	0	20.16
5	1.663	1.9	−19.57	0
6	2.722	5.4	0	9.92
7	2.913	4.1	−7.87	0
8	5.11	5.4	0	−9.81
9	5.213	5.4	−10.49	0
10	7.458	5.4	0	19.44
11	7.541	5.4	19.37	0
12	10.465	5.4	0	−2.46
13	10.546	5.4	−2.04	0
14	13.39	5.4	0	−16.84
15	13.448	5.4	16.8	0
16	15.227	5.4	−7.35	0
17	15.271	5.4	0	6.42
18	17.259	5.4	0	−9.58
19	17.316	5.4	9.09	0

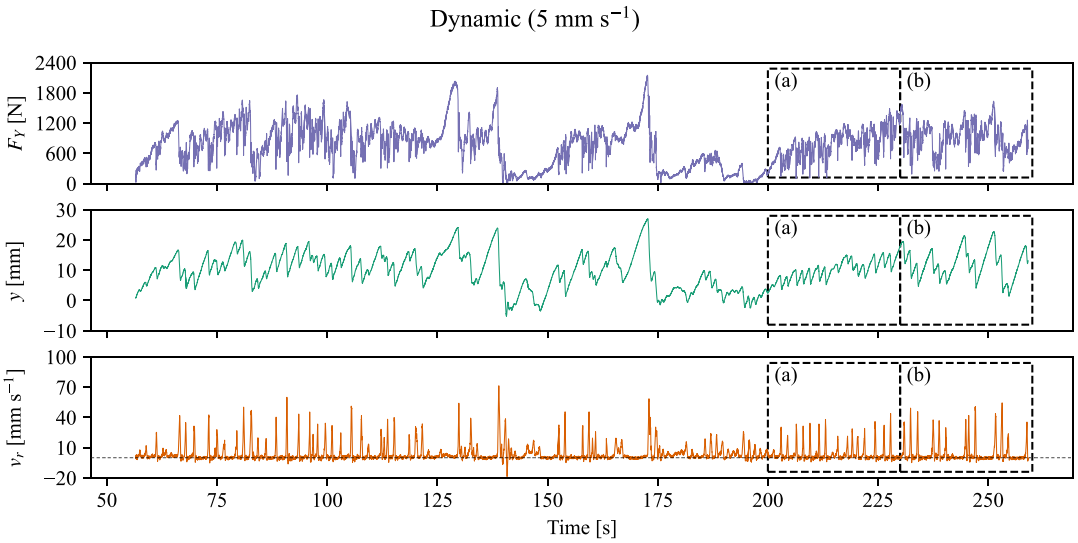

Fig. A.1. Force (F_Y)–displacement (y)–relative velocity (v_r) histories of the dynamic test at $v_d = 5\,\mathrm{mm\,s^{-1}}$. The dashed horizontal line indicates $v_r = 0\,\mathrm{mm\,s^{-1}}$. The extract a) was presented in Fig. 6a) and the extract b) was presented in Fig. 6b).

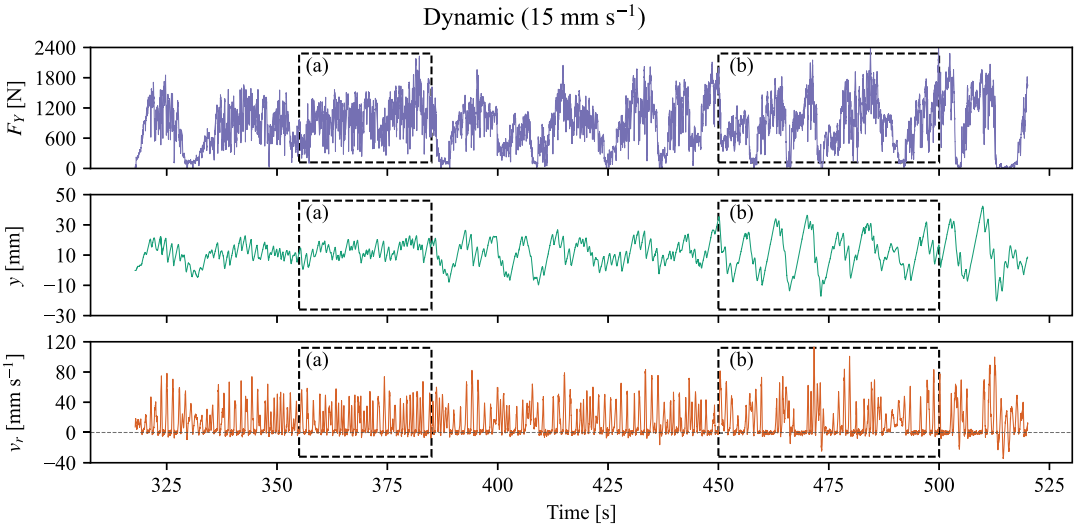

Fig. A.2. Force (F_Y)–displacement (y)–relative velocity (v_r) histories of the dynamic test at ice-drift speed $v_d = 15\,\mathrm{mm\,s^{-1}}$. The dashed horizontal line indicates $v_r = 0\,\mathrm{mm\,s^{-1}}$. The extract a) was presented in Fig. 6c) and the extract b) was presented in Fig. 7a).

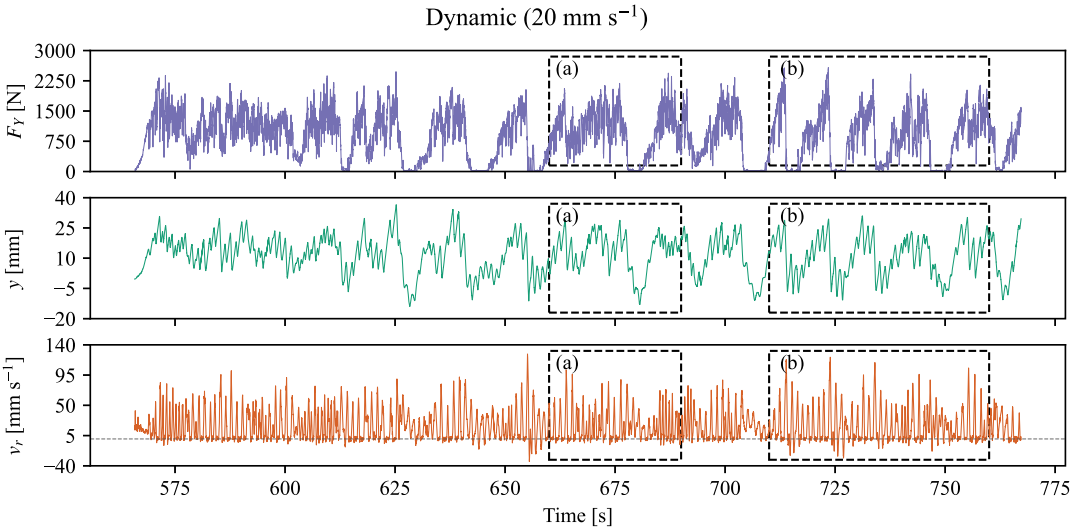

Fig. A.3. Force (F_Y)–displacement (y)–relative velocity (v_r) histories of the dynamic test at ice-drift speed $v_d = 20\,\mathrm{mm\,s^{-1}}$. The dashed horizontal line indicates $v_r = 0\,\mathrm{mm\,s^{-1}}$. The extract a) was presented in Fig. 6d) and the extract b) was presented in Fig. 7b).

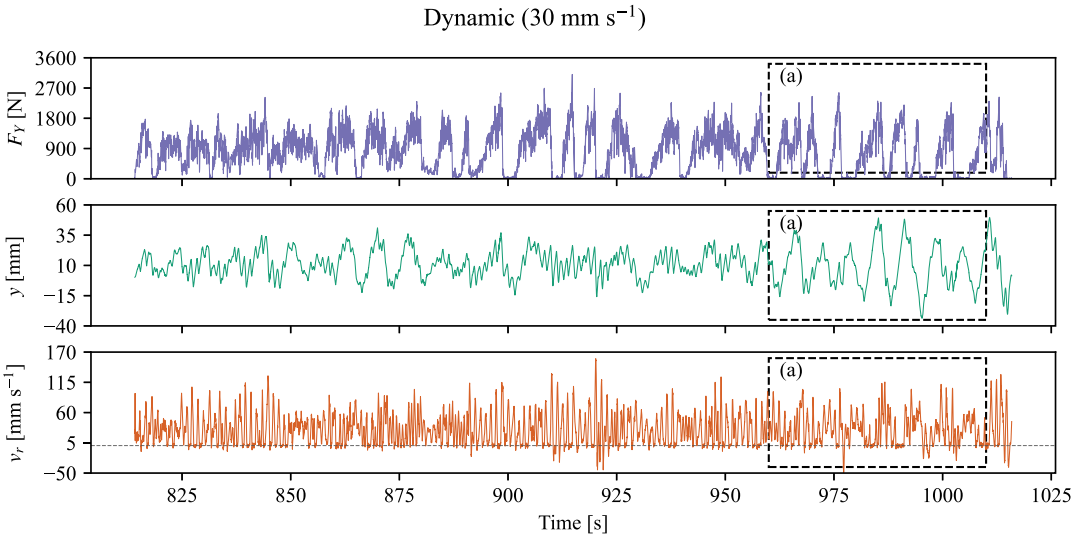

Fig. A.4. Force (F_Y)–displacement (y)–relative velocity (v_r) histories of the dynamic test at ice-drift speed $v_d = 30\,\mathrm{mm\,s^{-1}}$. The dashed horizontal line indicates $v_r = 0\,\mathrm{mm\,s^{-1}}$. The extract a) was presented in Fig. 7c).

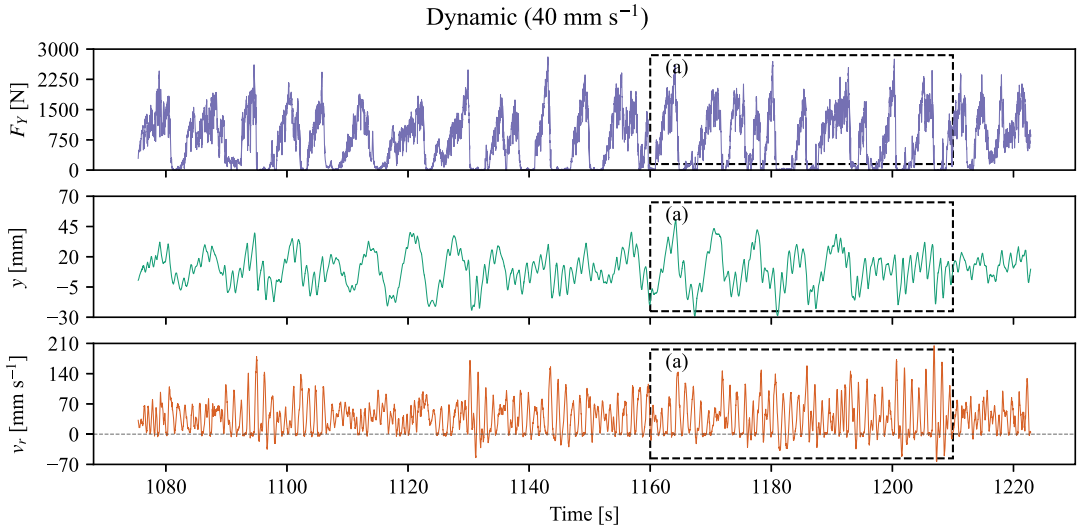

Fig. A.5. Force (F_Y)–displacement (y)–relative velocity (v_r) histories of the dynamic test at ice-drift speed $v_d = 40\,\mathrm{mm\,s^{-1}}$. The dashed horizontal line indicates $v_r = 0\,\mathrm{mm\,s^{-1}}$. The extract a) was presented in Fig. 7d).

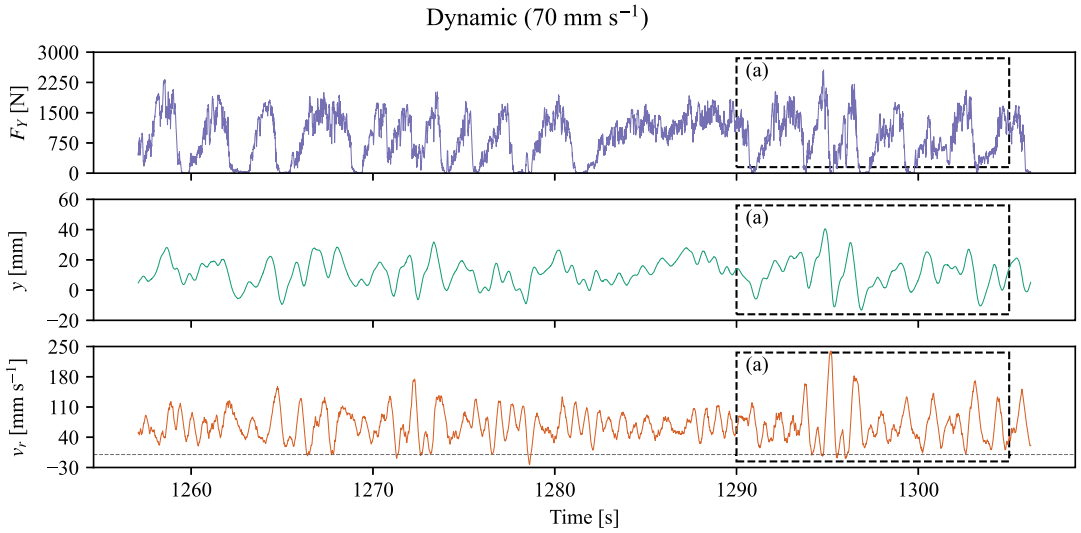

Fig. A.6. Force (F_Y)–displacement (y)–relative velocity (v_r) histories of the dynamic test at ice-drift speed $v_d = 70\,\mathrm{mm\,s^{-1}}$. The dashed horizontal line indicates $v_r = 0\,\mathrm{mm\,s^{-1}}$. The extract a) was presented in Fig. 8a).

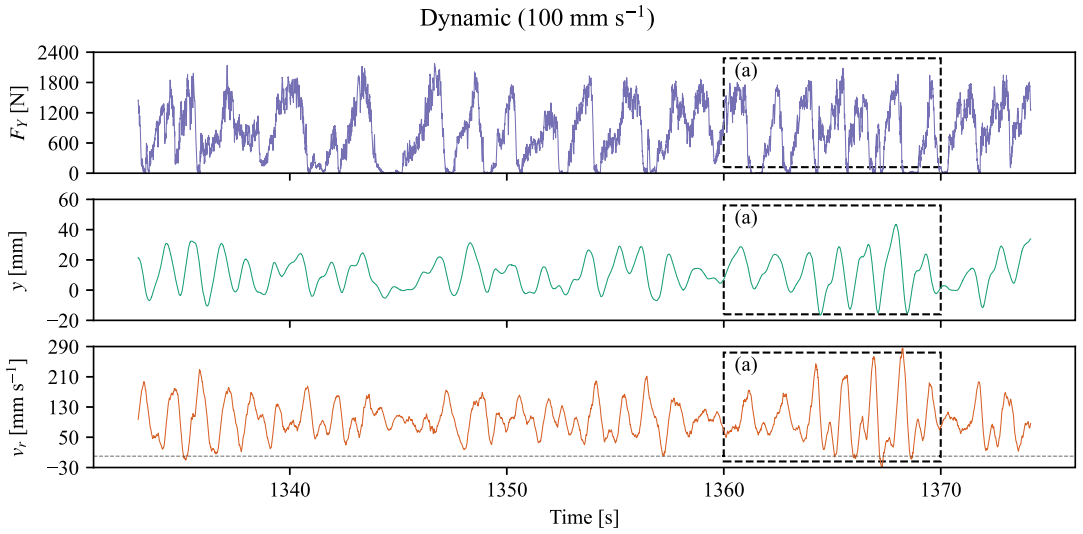

Fig. A.7. Force (F_Y)–displacement (y)–relative velocity (v_r) histories of the dynamic test at ice-drift speed $v_d = 100\,\mathrm{mm\,s^{-1}}$. The dashed horizontal line indicates $v_r = 0\,\mathrm{mm\,s^{-1}}$. The extract a) was presented in Fig. 8b).

Data availability

The experimental data can be obtained from Zenodo (https://doi.org/10.5281/zenodo.13899191).

References

[1] van der Stap Florian L, Nielsen Martin B, Owen Cody C, van der Male Pim, Hendrikse Hayo. On the feasibility of monopile foundations for offshore wind in the Baltic Sea. In: Proceedings of the 27th International Conference on Port And Ocean Engineering under Arctic Conditions. Glasgow, United Kingdom; 2023.
[2] Hammer Tim C, Willems Tom, Hendrikse Hayo. Dynamic ice loads for offshore wind support structure design. Mar Struct 2023;87:103335.
[3] Brown Thomas G, Määttänen Mauri. Comparison of Kemi-I and Confederation bridge cone ice load measurement results. Cold Reg Sci & Technol 2009;55(1):3–13.
[4] Barker Anne, Timco Garry, Gravesen Helge, Vølund Per. Ice loading on Danish wind turbines: Part 1: Dynamic model tests. Cold Reg Sci & Technol 2005;41(1):1–23.
[5] Gravesen Helge, Sørensen Søren L, Vølund Per, Barker Anne, Timco Garry. Ice loading on Danish wind turbines: Part 2. Analyses of dynamic model test results. Cold Reg Sci & Technol 2005;41(1):25–47.
[6] Wang Guojun, Zhang Dayong, Yue Qianjin, Yu Songsong. Study on the dynamic ice load of offshore wind turbines with installed ice-breaking cones in cold regions. Energies 2022;15(9):3357.
[7] Tian Yufeng, Huang Yan. The dynamic ice loads on conical structures. Ocean Eng 2013;59:37–46.
[8] Yue Qianjin, Bi Xiangjun. Full-scale tests and analysis of dynamic interaction between ice sheet and conical structures. In: Proceedings of 14th IAHR International Symposium on Ice, vol. 2, Potsdam, NY, USA; 1998, p. 939–45.
[9] Yue Qianjin, Bi Xiangjun. Ice-induced jacket structure vibrations in Bohai Sea. J Cold Reg Eng 2000;14(2):81–92.
[10] Wessels Egon, Kato Kazuyuki. Ice forces on fixed and floating conical structures. In: Proceedings of the 9th IAHR International Symposium on Ice. Sapporo, Japan; 1988, p. 666–91.
[11] Frederking Robert, Schwarz Joachim. Model tests of ice forces on fixed and oscillating cones. Cold Reg Sci & Technol 1982;6(1):61–72.
[12] Wessels Egon. Model test investigation of ice forces on fixed and floating conical structures. In: 7th IAHR International Symposium on Ice. Hamburg, Germany; 1984, p. 203–19.
[13] Sodhi Devinder S, Morris Carl E, Cox Gordon FN. Sheet ice forces on a conical structure: An experimental study. In: Proceedings of the 8th Conference on Port and Ocean Engineering under Arctic Conditions, vol. 2, Narssarssuaq, Greenland; 1985, p. 643–55.
[14] Kato Kazuyuki. Experimental studies of ice forces on conical structures. In: 8th IAHR International Symposium on Ice. IowaCity, Iowa, USA; 1986, p. 185.
[15] Huang Yan, Song An, Shi Qingzeng. The study of ice induced vibration on a compliant cone. In: Proceedings of the 18th International Conference on Port and Ocean Engineering under Arctic Conditions, vol. 3, Potsdam, NY, USA; 2006, p. 1217–28.
[16] Ziemer Gesa, Evers Karl-Ulrich, Voosen Christian. Influence of Structural Compliance and Slope Angle on Ice Loads and Dynamic Response of Conical Structures. In: Proceedings of the ASME 2015 34th International Conference on Ocean, Offshore and Arctic Engineering. vol. 8, St. John's, Newfoundland, Canada; 2015, Ian Jordaan Honoring Symposium on Ice Engineering, V008T07A037.
[17] Timco Garry W, Nwogu Okey G, Christensen Flemming T. Compliant model tests with the Great Belt West Bridge piers in ice Part I: Test methods and key results. Cold Reg Sci & Technol 1995;23(2):149–64.
[18] Xu Ning, Yue Qianjin, Qu Yan, Bi Xiangjun, Palmer Andrew. Results of field monitoring on ice actions on conical structures. J Offshore Mech Arct Eng 2011;133(4):041502.
[19] Kärnä Tuomo, Jochmann Peter. Field observations on ice failure modes. In: Proceedings of the 17th International Conference on Port and Ocean Engineering under Arctic Conditions. Trondheim, Norway; 2003.
[20] Hammer Tim C, Puolakka Otto, Hendrikse Hayo. Scaling ice-induced vibrations by combining replica modeling and preservation of kinematics. Cold Reg Sci & Technol 2024;220:104127.

[21] Hammer Tim C, Hendrikse Hayo. Hardware-in-the-loop experiments in model ice for analysis of ice-induced vibrations of offshore structures. Sci Rep 2024;14(1):18327.
[22] Hammer Tim C, Hendrikse Hayo. Experimental study into the effect of wind-ice misalignment on the development of ice-induced vibrations of offshore wind turbines. Eng Struct 2023;286:116106.
[23] Hammer Tim C, van Beek Kees, Koning Jeroen, Hendrikse Hayo. A 2D test setup for scaled real-time hybrid tests of dynamic ice-structure interaction. In: Proceedings of the 26th International Conference on Port and Ocean Engineering under Arctic Conditions. Moscow, Russia; 2021.
[24] Li Zhijun, Riska Kaj. Preliminary study of physical and mechanical properties of model ice. Technical report, Espoo, Finland: Helsinki University of Technology (TKK); 1996.
[25] Hendrikse Hayo, Hammer Tim C, van den Berg Marnix, Willems Tom, Owen Cody C, van Beek Kees, Ebben Nick JJ, Puolakka Otto, Polojärvi Arttu. Experimental data from ice basin tests with vertically sided cylindrical structures. Data Brief 2022;41:2352–3409.
[26] International Organization for Standardization. ISO 19906:2019(en) Petroleum and natural gas industries – Arctic offshore structures. Geneva, Switzerland: International Organization for Standardization; 2019.
[27] Määttänen Mauri, Järvinen Erkki. Baltic aids-to-navigation ice-induced vibration measurements 2003. Technical report, Helsinki University of Technology (TKK); 2003.
[28] Gagnon Robert. Spallation-based numerical simulations of ice-induced vibration of structures. Cold Reg Sci & Technol 2022;194:103465.
[29] Sodhi Devinder S. Crushing failure during ice–structure interaction. Eng Fract Mech 2001;68(17):1889–921.
[30] Neill Charles R. Dynamic ice forces on piers and piles. An assessment of design guidelines in the light of recent research. Can J Civ Eng 1976;3(2):305–41.
[31] Määttänen Mauri. Ice force design and measurement of a conical structure. In: Proceedings of the 12th IAHR International Symposium on Ice. Trondheim, Norway; 1994, p. 401–10.
[32] Kärnä Tuomo, Kolari Kari, Jochmann Peter, Evers Karl-Ulrich, Xiangjun Bi, Määttänen Mauri, Martonen Petter. Ice action on compliant structures: Laboratory indentation tests. Technical report, VTT Technical Research Centre of Finland; 2003.
[33] Muhonen Ari, Kärnä Tuomo, Järvinen Erkki, Riska Kaj, Lehmus Eila. Laboratory indentation tests with thick freshwater ice. Technical report, Helsinki University of Technology (TKK); 1992.
[34] Finn David W, Jones Stephen J, Jordaan Ian J. Vertical and inclined edge-indentation of freshwater ice sheets. Cold Reg Sci & Technol 1993;22(1):1–18.
[35] Petry Alice, Hammer Tim C, Polojärvi Arttu, Hendrikse Hayo, Puolakka Otto. Ice basin experiments on mixed-mode failure on ice cones. In: Proceedings of the 27th International Conference on Port and Ocean Engineering under Arctic Conditions. Glasgow, United Kingdom; 2023.
[36] Xu Ning, Yue Qianjin, Bi Xiangjun, Kärnä Tuomo, Zhang Dayong. Experimental study of dynamic conical ice force. Cold Reg Sci & Technol 2015;120:21–9.
[37] Finn David W. Vertical and inclined edge-indentation of freshwater ice sheets [Ph.D. thesis], Memorial University of Newfoundland, Canada; 1991.
[38] Ranta Janne, Polojärvi Arttu, Tuhkuri Jukka. Limit mechanisms for ice loads on inclined structures: Buckling. Cold Reg Sci & Technol 2018;147:34–44.
[39] Kornishin Konstantin A, Efimov Yaroslav O, Tarasov Petr A, Guzenko Roman B, Mironov Yevgeny U, Porubaev Victor S, Bekker Alexander T, Makarov Oleg A, Gogoladze Denis Z. Distributions of ice blocks composing ice ridges and stamukhas of the Kara, Laptev and East Siberian Seas. Int J Offshore Polar Eng 2025;35(01):10–8.
[40] Timco Garry W. Ice forces on structures: Physical modelling techniques. In: 7th IAHR International Symposium on Ice. Hamburg, Germany; 1984, p. 117–50.
[41] von Bock und Polach Rüdiger U Franz, Ettema Robert, Gralher Silke, Kellner Leon, Stender Merten. The non-linear behavior of aqueous model ice in downward flexure. Cold Reg Sci & Technol 2019;165:102775.
[42] Smirnov Victor N, Kovalev Sergey M, Znamensky Maxim S, Kolabutin Nikolay V, Kornishin Konstantin A, Efimov Yaroslav O, Pavlov Vladimir A. Instrumental real-time monitoring and prediction of sea ice compression and ridging. In: Proceedings of the 29th International Ocean and Polar Engineering Conference. Honolulu, Hawaii, USA: International Society of Offshore and Polar Engineers (ISOPE); 2019, p. 679–83.
[43] Smirnov Victor N, Kovalev Sergey M, Chernov Alexey V, Nubom Alexey A, Kolabutin Nikolay V, Shimanchuk Egor V, Kornishin Konstantin A, Efimov Yaroslav O, Tarasov Petr A. Large-scale ice crushing experiments with icebreaker. In: Proceedings of the 29th International Ocean and Polar Engineering Conference. Honolulu, Hawaii, USA: International Society of Offshore and Polar Engineers (ISOPE); 2019, p. 792–8.